International Journal of Multiphase Flow 35 (2009) 952–962

Contents lists available at ScienceDirect

International Journal of Multiphase Flow

journal homepage: www.elsevier.com/locate/ijmulflow

Application of the scale entropy diffusion model to describe a liquid atomization process

Christophe Dumouchel *, Sébastien Grout

CNRS UMR 6614 – CORIA, Université et INSA de Rouen, Avenue de l'Université – BP 12, 76 801 Saint Etienne du Rouvray, France

ARTICLE INFO

Article history:
Received 28 November 2008
Received in revised form 27 February 2009
Accepted 7 May 2009
Available online 15 May 2009

Keywords:
Liquid spray
Atomization process
Multiscale analysis
Scale entropy diffusion model

ABSTRACT

Whatever the situation, liquid atomization processes show a continuous evolution of the liquid system shape. However, such a system is a multiscale object, i.e., its shape cannot be fully described by a single geometrical parameter. The present work makes use of the scale entropy function to describe this multiscale object. This function is found similar to the scale distribution previously introduced to take into account the droplet shape in liquid spray characterization. Time-averaged scale entropy is locally measured on images of atomizing liquid flows issuing from a low injection pressure single-hole triple-disk nozzle. The advantage in using this nozzle is that the atomization process and the spray are inscribed in a plane and can be fully described by 2-D visualizations. The measurements are performed from the nozzle exit down to the spray region. The operating conditions consider varying injection pressure and liquid physical properties. The temporal evolution of the scale entropy is described by the scale entropy diffusion model. Initially developed in turbulence, this model introduces new parameters such as the scale diffusivity and the local scale entropy flux sink, which characterize the diffusion dynamic of the scale entropy in the scale space. For the first time, these parameters are measured and strong correlations between them and the working conditions are evidenced. Furthermore, new parameters are introduced such as a scale viscosity and the total scale entropy flux lose. These results demonstrate the relevance of the scale entropy diffusion model to describe a liquid atomization process. This application is the first of its kind.

1. Introduction

The most encountered liquid spray production process consists in ejecting a liquid flow into a gaseous environment. Free of any parietal constraints, the liquid flow issuing from the nozzle deforms thanks to the growth of perturbations. Perturbation growth stretches the liquid until fragments detach from the bulk flow. According to the situation these fragments may experience an equivalent process and disintegrate into smaller fragments and so on until the surface tension cohesion forces are great enough to prevent from further disintegration. During the whole mechanism, the ratio of surface to mass in the liquid is increased (Mansour and Chigier, 1991).

Three major factors control a liquid atomization process, namely, the initial shape of the liquid flow, the presence of initial disturbances and mechanisms that allow some of these disturbances to grow until disintegration occurs. The characteristics of the resulting spray depend on these factors. The issuing flow characteristics, and therefore the choice of the injector nozzle, are of paramount important since they control the initial shape of the liquid flow. Furthermore, this flow may also convey initial disturbance sources through the presence of velocity fluctuations, boundary layers, turbulent structures or cavitation for instance. According to the situation, surface tension forces, aerodynamic forces, shear stress or momentum exchange between the two phases can pilot disturbance growth. As emphasized in a recent review (Dumouchel, 2008), in most situations, several perturbations, characterized by a wide range of characteristic time and length scales, emerge during an atomization process explaining why spray droplets are highly dispersed in size. Furthermore, because of the implication of issuing liquid flow characteristics such as those mentioned above, an atomization mechanism is intermittent. Thus, the characterization and analysis of liquid flow distortions during an atomization mechanism are difficult tasks at the origin of a lack of a universal atomization model so far.

The literature abounds in atomization mechanism visualizations (Dumouchel, 2008 for instance). Whatever the situation, an atomization mechanism can be seen as a continuous evolution of the shape of a liquid system. However, an atomizing liquid system is a geometric object with a complex boundary: thus its shape description requires sophisticated tool such as the concept of fractal dimension introduced by Kolmogorov (Hunt and Vassilicos, 1991) generalized by Mandelbrot (1982) and extensively used to

* Corresponding author. Tel.: +33 232953623.
E-mail address: Christophe.Dumouchel@coria.fr (C. Dumouchel).

0301-9322/$ - see front matter © 2009 Elsevier Ltd. All rights reserved.
doi:10.1016/j.ijmultiphaseflow.2009.05.002

investigate fluid turbulence (Sreenivasan and Meneveau, 1986). The fractal dimension is an extension of the Euclidean dimension and allows describing complex boundaries. It is a measure of the tortuosity, fragmentation or roughness of a surface or a line that is self-similar over a range of scales, i.e., that presents similar structures when observed at different magnifications. Fractal analysis is used in different fields (physics, medicine, etc.). Surprisingly the application of fractal analysis to study the morphology of atomizing liquid systems has received very little attention so far.

The first application of fractal analysis to describe the primary breakup process of a liquid flow is due to Shavit and Chigier (1995) who considered the liquid gas interface of an air assisted cylindrical liquid jet. They found that such an interface is a fractal within a range of scale and that the fractal dimension increases, reaches a maximum and decreases as the distance from the nozzle increases. The fractal dimension is a maximum in the region where the drop production is the most effective. Shavit and Chigier (1995) also reported that this maximum was related to the breakup length and to a spray mean drop-diameter. According to the authors, the fractal nature of the interface of air-assisted liquid jets is a consequence of the interaction of the air turbulence and its eddy structure with the liquid gas interface. The relevance of using fractal analysis to characterize an atomization process was confirmed by a second investigation (Dumouchel et al., 2005b) that considered liquid stream issuing from low injection pressure simplified cavity nozzles. Contrary to the situations examined by Shavit and Chigier (1995), such atomization processes are characterized by low Weber numbers revealing the negligible influence of the aerodynamic forces on the atomization process. In this case, liquid turbulence initiates interface disturbances and surface tension forces govern the liquid system distortion and fragmentation (Dumouchel et al. 2005a). This second investigation led to similar conclusions as those obtained by Shavit and Chigier (1995). A more recent work due to Grout et al. (2007) reconsidered this investigation. It was demonstrated that the best fractal analysis method to be used to locally analyze atomizing liquid flow is the Euclidean Distance Mapping (EDM). (Shavit and Chigier (1995) and Dumouchel et al. (2005b) used the box counting method.) EDM provides an analysis over a wider scale interval. Although Grout et al. (2007) retrieved a self-similarity of the interface over a limited scale interval, their results evidenced a scale and time-dependent fractal dimension over the scale interval covered by the liquid system.

It is interesting to quote here the work due to Yon et al. (2004) that reports a morphological analysis of a cylindrical liquid jet in the Rayleigh regime and perturbed at a controlled frequency. A scale distribution measured on 2-D images characterized the liquid jet shape evolution during the atomization process. The temporal evolution of this distribution allowed the temporal growth rate as well as the wavelength of the Rayleigh regime to be retrieved. This scale distribution was equivalent to a scale-dependent fractal dimension.

Thus, the evolution of the morphology of an atomizing liquid system must be associated to a scale and time-dependent fractal dimension. We propose in this paper to investigate the relevance of the scale entropy diffusion model due to Queiros-Conde (2003) to describe this phenomenon. This model, summarized in the next section, derives from the entropic-skins geometry formalism initially developed to describe intermittency in fully developed turbulence (Queiros-Conde, 1999, 2000, 2001). It introduces new concepts such as the scale diffusivity parameter and the scale entropy flux sink that control the mechanism of scale entropy diffusion in the scale space. The objective of this work is to apply this concept to describe an atomization process and to determine the scale diffusivity parameter and the scale entropy flux sink for this application. The experimental part of the work is presented in Section 3 and the results and application of the model constitute Section 4.

2. The scale entropy diffusion model

The scale entropy diffusion model was developed by Queiros-Conde (2003) to characterize turbulent interfaces. The following presentation of this model is a summary of what is detailed in reference (Queiros-Conde, 2003).

Let us consider a multiscale system noted Ω (such as a 3-D interface for instance) and characterized by a total volume V_T and a characteristic length l_0 called the reference scale of the system. V_T and l_0 are assumed to be correlated with each other as $V_T = l_0^d$ where d is the embedded dimension of the system. Let us now consider a part of Ω, called Ω_i, and defined as the part of the system Ω described by covering it with elements whose characteristic length scale is equal to l_i. The number N_i of elementary elements required to cover Ω is assumed to be dependent on the scale l_i as follows:

$$N_i \propto l_i^{-\delta_i} \tag{1}$$

where δ_i is a local fractal dimension in the scale space, i.e., the fractal dimension δ_i is a function of the scale l_i. Over the scale range covered by the system, δ_i varies from $d-1$ to d. The volume V_i of the system Ω_i is:

$$V_i \propto N_i l_i^d \propto l_i^{d-\delta_i} \tag{2}$$

The volume ratio V_i/V_T represents the volume fraction of the system Ω_i compared to the whole system. On the other hand, the volume ratio V_T/V_i represents the number of volume V_i required to fully cover the volume V_T. Queiros-Conde (2003) introduces the scale entropy $\Sigma_{i,0} = \ln(V_T/V_i)$ in order to quantify the level in disorder of Ω_i relative to Ω: Ω_i is more localized inside Ω implies that $\Sigma_{i,0}$ is higher. The scale entropy is a global quantity that decreases when the scale l_i increases towards the reference scale l_0. Using the above equations, we can write:

$$\Sigma_{i,0} = \ln\left(\frac{V_T}{V_i}\right) \propto \ln\left(\frac{l_0^d}{l_i^{d-\delta_i}}\right) \propto (\delta_i - d)\ln(l_i) \tag{3}$$

The evolution of the scale entropy in the logarithm scale space is proportional to the local fractal dimension. In order to quantify how scale entropy cascades through scale space, one introduces the scale entropy flux ϕ_i:

$$\phi_i = \frac{\Sigma_{i,0} - \Sigma_{i-1,0}}{\ln\left(\frac{l_i}{l_0}\right) - \ln\left(\frac{l_{i-1}}{l_0}\right)} \tag{4}$$

with $l_i < l_{i-1}$. Contrary to $\Sigma_{i,0}$, ϕ_i is a local quantity in the scale space. Assuming that l_{i-1} and l_i are close enough to assume a constant fractal dimension δ_i for scales belonging to $]l_i; l_{i-1}]$, Eq. (4) can be rewritten as:

$$\phi_i = \delta_i - d \tag{5}$$

The scale entropy flux is similar to the local fractal dimension δ_i. In other words, a purely fractal system (δ_i = cte) has a constant scale entropy flux. As δ_i varies from $d-1$ to d, ϕ_i varies from -1 to 0. Eqs. (4) and (5) are rewritten using new notations, namely, $x = \ln(l_i/l_0)$, $\Sigma(x) = \Sigma_{i,0}$ and $\phi(x) = \phi_i$, it comes:

$$\phi(x) = \frac{d\Sigma(x)}{dx} = \delta(x) - d \tag{6}$$

The flux variation throughout the scale space and expressed by Eq. (6) results from a sink of scale entropy flux which is quantified by introducing a scale entropy flux sink $\omega(x)$ defined by a unit of

scale logarithm (it is in fact a scale entropy flux density). Throughout the scale space, the scale entropy flux continuity between x and $x + dx$ is expressed by:

$$\phi(x+dx) - \phi(x) - \omega(x)dx = 0 \tag{7}$$

The flux that enters at x ($-\phi(x)$, remember that ϕ is negative) is equal to the issuing flux at $x + dx$ ($-\phi(x + dx)$) plus the flux lost in this scale interval ($\omega(x)dx$).The combination between Eqs. (6) and (7) leads to the following relationship between the scale entropy and the scale entropy flux sink:

$$\frac{d^2\Sigma(x)}{dx^2} - \omega(x) = 0 \tag{8}$$

A purely fractal system is characterized by a constant scale entropy flux (see Eq. (6)) and therefore corresponds to a scale entropy flux sink $\omega(x) = 0$ (all over the scale range for which the system is fractal). In other words, systems with a scale-dependent fractal dimension are characterized by the existence of a function $\omega(x)$ whose form is not imposed and can remain general. Using experimental results of the literature, Queiros-Conde (2003) showed that turbulent interfaces could be described by a uniform scale entropy flux sink in the scale space, i.e., $\omega(x) = \text{cte}$. Le Moyne et al. (2008) adopted a similar approach to characterize sprays produced by a diesel injector. In the present paper, this function is determined for a specific atomization mechanism.

Queiros-Conde (2003) emphasizes the analogy between Eq. (8) and the one-dimensional conduction equation: the scale entropy $\Sigma(x)$ would correspond to the temperature, the scale entropy flux $\phi(x)$ to a quantity proportional to a heat flux and $\omega(x)$ to a quantity proportional to a volumetric heat sink, which would be space dependent. He then considered the more general situation where the scale entropy $\Sigma(x)$ of the system is also time dependent and becomes $\Sigma(x, t)$. This case occurs when the local fractal dimension is time dependent ($\delta(x, t)$) due to non-stationary fluctuations or for some experiments where multiscale construction is observed in time. In this case, the scale entropy flux sink becomes also time dependent ($\omega(x, t)$) and carrying the analogy with heat equation, Queiros-Conde (2003) suggests describing time-dependent scale entropy with the following diffusion equation:

$$\frac{\partial^2\Sigma(x,t)}{\partial x^2} - \omega(x,t) = \frac{1}{\chi}\frac{\partial\Sigma(x,t)}{\partial t} \tag{9}$$

where χ, the scale diffusivity, characterizes diffusion of scale entropy through scale space. Queiros-Conde (2003) examined the simplified case where the term $\partial^2\Sigma(x, t)/\partial x^2$ is small compared to the two other terms for a given scale range $[l_i; l_0]$. In this scale range, the fractal dimension becomes mainly time dependent and indicates a local fractal feature of the object ($\delta(x, t) \approx \delta(t)$) and the term $\partial^2\Sigma(x, t)/\partial x^2$ can be omitted in Eq. (9). This reduced diffusion equation indicates that the temporal decrease of the scale entropy flux, which is conditioned by the scale diffusivity χ, is balanced by the scale entropy flux sink. (In a heat diffusion problem, this would correspond to a situation where there is no energy exchange since the storage energy is equal to the locally produced energy.) By modeling the scale entropy flux sink as $\omega(x, t) = (\delta_0 - \delta(t))/|x|$ where δ_0 is the fractal dimension imposed at scale l_0 by an external mechanism, and by using Eqs. (6) and (9), Queiros-Conde (2003) obtained the following fractal dimension temporal evolution in this simplified case:

$$\delta(t) = \delta_0 - (\delta_0 - \delta(t=0))e^{-\frac{t}{\tau^*}} \tag{10}$$

where the characteristic time $\tau^* = |x|^2/\chi$. Queiros-Conde (2003) found this simplification appropriate to characterize scalar passive turbulent interface.

3. Experimental work

3.1. Experimental setup and diagnostic

This section summarizes the experimental setup and diagnostic since details can be found elsewhere (Grout et al. 2007; Dumouchel et al. 2008a, 2008b). The liquid to be atomized is kept in a pressurized closed tank. The liquid feeding line is composed of a filter, a valve to control the liquid flow rate and a manometer that measures the injection pressure ΔP_i just upstream the injector. Table 1 presents the four liquids used within this work together with their physical properties. The injection pressure is kept low and ranges from 0.15 to 0.5 MPa except for heptane, the lowest surface tension fluid, for which it varies from 0.05 to 0.25 MPa.

All the experiments are conducted with a unique injector that has a single discharge orifice. The injector nozzle is a triple-disk nozzle whose geometry is inspired from compound injector encountered in low-pressure port-fuel injection engines. Fig. 1a and b provides a sketch of the triple-disk nozzle whose dimensions are given in Table 2. The liquid enters disk 1, expands in the cavity disk (disk 2) and discharges through disk 3 orifice. As soon as the liquid issues from the nozzle, the flow expands in the (O, x, z) plane and stretches as a 2-D liquid sheet. (Evidences of the 2-D organization are available in Dumouchel et al. (2005a).) Perturbations of different characteristic length-scale appear on the sheet edges in the near nozzle region. At this stage, small droplets might detach from the liquid sheet edges. Further downstream, the sheet more and more deforms and reorganizes as a ligament network that eventually breaks into droplets. As demonstrated in a previous investigation (Dumouchel et al. 2005a), two main characteristics of the liquid flow at the nozzle exit are responsible for this behavior. The nozzle internal geometry imposes drastic flow deflections and favors the development at the exit section of a counter-rotating double-swirl, characterized by a non-axial kinetic energy, as well as a consistent turbulent level. The double-swirl is responsible for the flow 2-D stretch in the ($0, x, z$) plane and the turbulence initiates perturbations. As going downstream, the double-swirl effect weakens and liquid sheet contraction occurs due to surface tension forces. The effect of this contraction is conditioned by the deformation initially imposed by the turbulence and results in the ligament network production. The rather good efficiency of this atomization mechanism is due to the shaping of the issuing liquid flow as a flat liquid sheet: the characteristic length scale of a sheet (its thickness) being less than the one of cylindrical jet (its diameter) that would produce the injector in the absence of the double-swirl structure. Some typical characteristics of the flow issuing from the nozzle are given in Table 1, namely, the discharge coefficient

Table 1
Liquid physical properties (percentages indicate weight proportion), discharge coefficient C_D, gaseous Weber number We_G and Reynolds number Re (We_G and Re are those corresponding to the maximum injection pressure, i.e., 0.25 MPa for heptane and 0.5 MPa for the other liquids).

Liquid	ρ_L (kg/m^3)	μ_L (kg/ms)	σ (N/m)	C_D (–)	We_G (–)	Re (–)
Heptane	740	0.41×10^{-3}	0.0206	0.63	2.7	5300
Water	991	1.00×10^{-3}	0.0720	0.63	1.3	3700
Water–ethanol 1%	986	1.01×10^{-3}	0.0659	0.61	1.3	3500
Water–ethanol 10%	972	1.43×10^{-3}	0.0461	0.61	1.9	2500

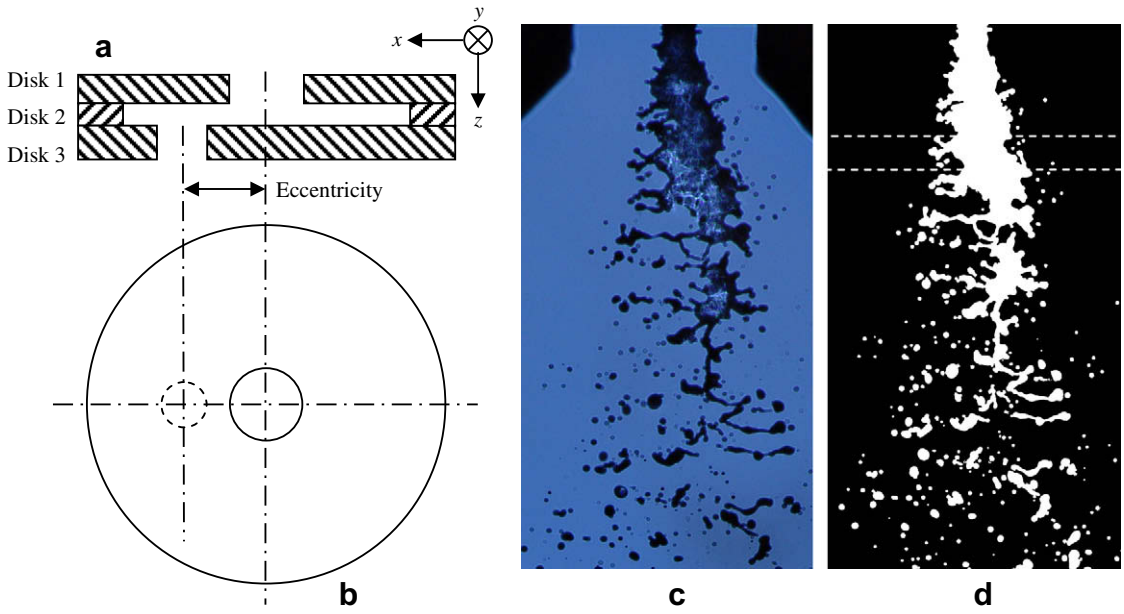

Fig. 1. Geometry of the injector nozzle and visualization of the atomization mechanism. (a) Nozzle side view and coordinate system, (b) nozzle top view, (c) image of the flow issuing from the nozzle (water, $\Delta P_i = 0.4$ MPa, (0; x; z) plane), and (d) corresponding two gray-level silhouette image and position of the analyzing window at $t_0 = 115.9$ μs.

Table 2
Injector triple-disk nozzle dimensions.

	Thickness (μm)	Hole diameter (μm)	Eccentricity (μm)
Disk 1	177	300	0
Disk 2	75	2254	0
Disk 3	76	180	200

C_D, the gaseous Weber number We_G and the Reynolds number Re defined by:

$$C_D = \frac{4Q_v}{\pi d_{or}^2 \sqrt{\frac{2\Delta P_i}{\rho_L}}}, \quad We_G = \frac{\rho_G V_q^2 d_{or}}{\sigma}, \quad Re = \frac{\rho_L V_q d_{or}}{\mu_L} \tag{11}$$

where Q_v is the volume flow rate, d_{or} the nozzle orifice diameter, ρ_L and ρ_G (=1.2) the liquid and gas density, respectively, V_q the average axial velocity, σ the surface tension and μ_L the liquid dynamic viscosity. The volume flow rate was measured by weighting the amount of liquid collected during a controlled time interval and the average velocity was calculated by dividing the volume flow rate by the nozzle orifice section. The Weber and Reynolds numbers shown in Table 1 are those obtained for the maximum injection pressure. It is interesting to consider the Weber numbers, which is the ratio between the aerodynamic forces and the cohesion surface tension forces. As demonstrated in a previous investigation (Dumouchel et al. 2005a), the low Weber numbers (<3) indicate a negligible contribution of the aerodynamic forces to the atomization mechanism that is mainly controlled by the surface tension forces.

As described above, the atomization mechanism is orientated in the (O, x, z) plane, i.e., all liquid structures and droplets are inscribed in this plane. Thus, investigation of this mechanism can be satisfactorily approached by 2-D visualizations. Images of the flow are taken in the (O, x, z) plane only. A backlight arrangement is chosen. The light source has a very short pulse-duration (11 ns) in order to freeze the liquid system. A camera with a high number of pixels (3040×2016 pixel^2) is used to reach a good spatial resolution. The image covers a field of 10.5×7 mm^2 corresponding to a spatial resolution equal to 3.47 μm/pixel. Considering the greatest liquid velocity, the maximum displacement during the flash duration is equal to 0.29 μm that is far less than the distance covered by 1 pixel. Thus, the images show very well frozen liquid flow and spray for each working condition. An example of image is shown in Fig. 1c. The optical arrangement provides a depth of field equals to 7 mm. This depth is much greater than the thickness of the atomizing liquid flow. Thus, no liquid fragments and droplets are out-of-focus and they are all visualized with a very good contrast. Finally, 150 images are taken and analyzed for each working condition.

3.2. Image treatment

The image treatment consists in making two gray-level images. The objective of the analysis is to investigate the liquid atomization mechanism from the nozzle exit down to the spray region. In consequence and contrary to what was done in a previous investigation (Grout et al. 2007) all the liquid is taken into account in the present analysis, namely, the continuous liquid flow attached to the nozzle (continuous liquid phase) as well as all detached ligaments and droplets (dispersed liquid phase). Furthermore, as we concentrate on the liquid phase only, the two gray-level images we produced are silhouette images where the liquid phase appears in white on a black background. The image treatments developed to segregate liquid pixels from background pixels have been detailed in Grout et al. (2007) and Dumouchel et al. (2008b) for the continuous and dispersed liquid phases, respectively.

The detection of the continuous liquid phase is performed on the blue frame of the image since its gray-level distribution reported the largest dynamic. A double-threshold technique was used. Furthermore, a dilation-erosion step was applied to limit the production of extra liquid–gas interface tortuosity caused by light refraction through the liquid flow (refer to Grout et al. (2007) for more details). The detection of the dispersed liquid phase is performed on the green frame. Contrary to the continuous liquid phase detection, a single threshold is used to segregate liquid and background pixels. Furthermore, because of slight contrast difference from one image to another, a threshold is determined for each individual image from the analysis of the gray-level distribution. As mentioned above, no liquid structures, fragments

or droplets are out-of-focus since they are all inscribed in the visualization plane. This ensures sharp gray-level gradients at the liquid–gas interface and therefore a phase segregation procedure insensitive to the choice of the threshold provided that this threshold was reasonably varied.

Before conducting the image analysis, a couple of tests are performed on each detected element of the dispersed liquid phase. First, groups of pixels less than 6 pixels are removed. Thus, the minimum detectable drop equivalent diameter D' (calculated by surface conservation) is fairly less than 10 μm. Second, light scattered by the drops may have two undesirable effects. On big drops, some internal pixels might be identified as background pixels. These pixels are easily identifiable and given the liquid gray-level value. On small droplets, light scattering might result in bad encoded drops and produce separated groups of pixels. These groups of pixels are characterized by a small equivalent diameter D' and a low circularity parameter C defined as 4 multiplied by the ratio of the surface area to the square of the perimeter. This circularity varies from 0 to 1, the latter value corresponding to a circle. Because the surface tension cohesion forces are inversely proportional to the drop diameter, small liquid droplets are expected to be spherical and characterized by rather high circularity C. After several tests, we obtained a condition to identify non-circular small objects that corresponded to badly encoded droplets: all groups of pixels such that $D' < 75 - 60C$ (where D' is expressed in μm) were removed. Fig. 1d shows the two gray-level silhouette image of the initial image shown in Fig. 1c.

3.3. Image analysis

The study of the whole atomization mechanism, i.e., from the nozzle exit down to the spray, is performed by conducting local analysis of the shape of the liquid system. To achieve this, portion of the liquid phase delimited by a rectangular Analyzing Window (AW) is analyzed as a function of the position of this window. The height of the window is $h_{AW} = 200$ pixels and its position is located by the distance d_{AW} from the nozzle exit and the analyzing window middle line. (Fig. 1d shows the analyzing window.) The choice of the height h_{AW} might be critical and will be discussed later. Note that at positions where the analyzing window intercepts the continuous liquid phase, it delimits portion of liquid interface that constitute "open" objects. It was demonstrated (Grout et al. 2007) that the best appropriate fractal analysis method to characterize the shape of such objects is the Euclidean Distance Mapping (EDM) method. This method is used in the present analysis.

EDM is a sausage method that has been described in many references (see Bérubé and Jébrak (1999) for instance). Its application to the present silhouette images can be summarized as follows. Let us consider the presence of N objects in the Analyzing Window. These objects can be detached ligaments, droplets or a portion of the continuous liquid phase. Each object delimits a surface area noted S_i so that the total surface area S_T covered by the liquid phase in the Analyzing Window is given by:

$$S_T = \sum_{i=1}^{N} S_i \tag{12}$$

Each object contained in the Analyzing Window is described as follows. We consider the line defined by the inner points all located at a given distance r (called scale) from the object boundary. The surface area $S_i(r)$ comprised between this line and the object boundary is measured as a function of the scale r. We introduce the reference scale r_i of the object i as the smallest scale r that allows the object to be fully covered, i.e., $S_i(r_i) = S_i$. For any scale greater than the reference scale, the delimited surface $S_i(r)$ is kept constant and equal to S_i. Then, for the set of N objects contained in the Analyzing Window, we introduce the total surface area $S(r)$ at scale r defined as the contribution of each object at this scale, namely:

$$S(r) = \sum_{i=1}^{N} S_i(r) \tag{13}$$

If the function $S(r)$ reports a dependence with the scale r of the form:

$$S(r) = Kr^{(2-\delta)} \tag{14}$$

where K is a constant, the liquid system is a fractal object and δ is its fractal dimension. Thus, the plot of $S(r)$ as a function of r in a log–log scale would report a linear correlation. This plot is the Richardson–Mandelbrot plot. The determination of the fractality of an object or a system can go through the analysis of the local slope of a Richardson–Mandelbrot plot, i.e., the slope as a function of the scale (Panico and Sterling, 1995; Guessasma et al., 2003): the object is fractal if the local slope sustains a constant value over a spatial scale range bounded by the inner and outer cutoff scales and the corresponding fractal dimension can be extracted from the slope.

In the present study, the function $S(r)$ is measured for several positions of the Analyzing Window on each image. However, since the experimental protocol does not provide a temporal resolution of the liquid system behavior, the representative spatial evolution of this function requires a temporal averaging based on the analysis of the 150 images available for each operating condition. To perform this averaging, we must pay attention to the fact that, for a given operating condition and a given Analyzing Window position d_{AW}, the total surface area of the liquid phase may differ from one image to another. To overcome these problems, the local shape of the liquid system is characterized by the new function $S(r)$ defined by:

$$S(r) = \frac{\sum_{j=1}^{150} \left(\frac{S(r)}{S_T}\right)_j}{150} \tag{15}$$

where the index j refers to the image number. The function $S(r)$ evolves from 0 to 1 and is similar to a cumulative distribution. In previous investigations (Dumouchel et al. 2008a,b) this function, called the cumulative surface-based scale distribution, was used to characterize liquid spray droplets. Contrary to the traditional drop-diameter distributions, $S(r)$ is explicitly dependent on the shape of the droplets. To be consistent with these previous investigations, the scale r is replaced by the scale $D = 2r$ in the following (thus the reference scale of a circular object is equal to its diameter). If, in average, the liquid system is a fractal object with a fractal dimension δ, a similar equation as Eq. (14) stands for the cumulative surface-based scale distribution, namely:

$$\ln(S(D)) \propto (2 - \delta)\ln(D) \tag{16}$$

4. Results and application of the model

Fig. 2 shows an example of measured cumulative surface-based scale distributions (water, $\Delta P_i = 0.4$ MPa). $S(D)$ is presented as a function of the equivalent time t defined by $t = d_{AW}/V_q$. The physical representativeness of this equivalent time requires a rather constant velocity of the liquid that is framed by the image. It can be first shown that the Froude numbers $Fr = V_q/\sqrt{gL}$ where g is the acceleration due to gravity and L a characteristic length of the problem (taken here equal to the length covered by the image) are always greater than about 30. Thus, the variation of velocity due to gravity is negligible. Second, liquid velocity may vary also because of air drag forces: these forces cause the smaller drops

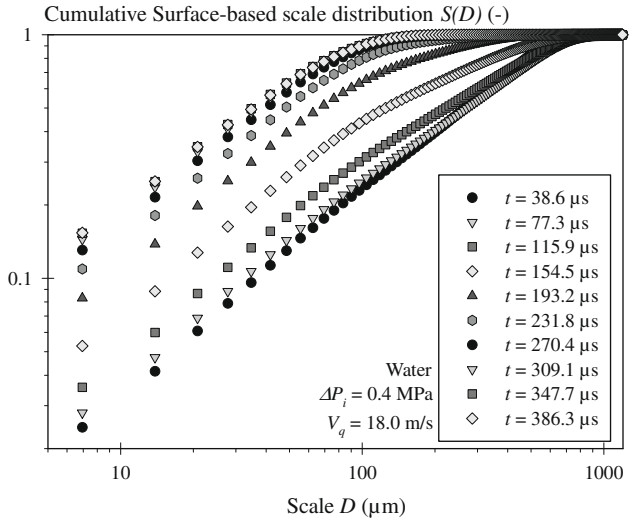

Fig. 2. Temporal evolution of the surface-based scale distribution $S(D)$ (water, $\Delta P_i = 0.4$ MPa).

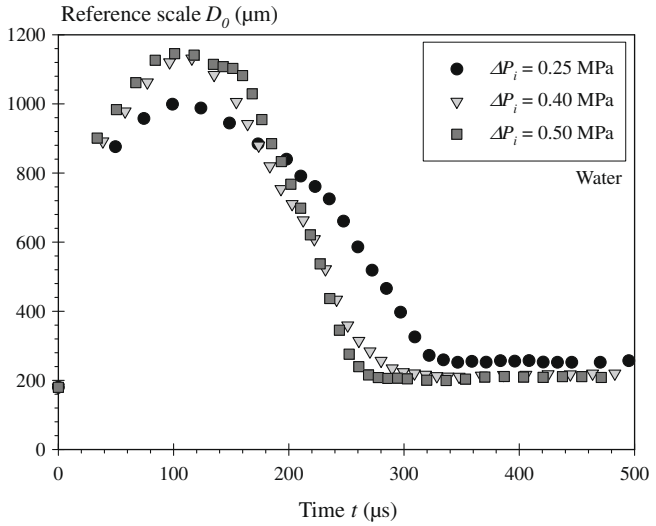

Fig. 3. Temporal evolution of the reference scale D_0 (water, influence of the injection pressure).

to lose velocity more rapidly than the larger droplets or the continuous liquid phase. This phenomenon was quantified by Rizk and Lefebvre (1984). For working conditions similar to those of the present work, they found that, at 10 mm from the injector, the reduction of velocity of drops greater than 100 µm never exceed 10% and is of the order of 30% for 40 µm drops. In consequence, the reduction of velocity of the small drops is not negligible. However, measurements performed in the spray (bottom of the images) revealed that the surface-fraction represented by the drops with diameter less than 50 µm never exceed 10%. Thus, these drops have a small contribution to the cumulative surface-based scale distribution and we assume that the equivalent time is suitable for the purpose of the work. This equivalent time is now used instead of the position throughout the paper.

The smallest time shown in Fig. 2 corresponds to the position of the Analyzing Window that is the closest to the nozzle exit ($d_{AW} = 0.7$ mm) and the greatest time corresponds to the window localized in the spray region. As expected $S(D)$ increases monotonously from 0 to 1 in the scale space. The limit 1 is reached at the reference scale D_0 of the system, i.e., the smallest scale required to fully cover the liquid system. In the small scale region ($D < 30$ µm), $S(D)$ reports a 'parallel increase' with time that illustrates the increase of surface fraction covered at these scales during the atomization mechanism, i.e., the emergence of smaller and smaller liquid structures. When $t > 300$ µs, the scale distribution is not time-dependent anymore and characterizes the final spray.

The reference scale D_0 varies with time as illustrated in Fig. 3. (D_0 is estimated as the smallest scale for which the first derivative of the curves shown in Fig. 2 is less than 0.01.) At $t = 0$, the liquid is at the nozzle exit section where the reference scale is equal to the diameter of the orifice, i.e., 180 µm. When time increases, D_0 increases, becomes a maximum D_{0Max} and decreases to finally reach a constant value D_{0Spray}. The increase of D_0 at the nozzle exit is a manifestation of the liquid system stretching in the plane of observation due to the action of the issuing flow double-swirl structure. This evolution is controlled by the dynamic of the issuing flow and depends on the injection pressure. The maximum reference scale D_{0Max} is reached when the stretching process ends because of modifications of the liquid system shape imposed by surface tension forces. At this stage, liquid gulfs and ligaments are created and prevent any further increase of the reference scale. Then, the intensification of the atomization mechanism leads to the formation of smaller and smaller liquid structures, which is represented by a continuously decreasing reference scale. The asymptotic value D_{0Spray}, which corresponds to the reference scale of the spray, is reached when the atomization process is completed. The scale D_{0Spray} and the time at which it is reached are both functions of the injection pressure as illustrated in Fig. 3. They are also dependent on the liquid physical properties. Finally, it is interesting to note in this figure that an increase of the scale D_{0Max} is accompanied by a decrease of the scale D_{0Spray}. This behavior makes sense since an increase of D_{0Max} reveals a decrease of the thickness of the liquid sheet and thinner liquid sheets produce smaller drops.

The distribution $S(D)$ offers a multiscale description of the atomization mechanism by quantifying, at each time, the participation of each scale on the whole system shape. The interesting result in Fig. 2 is that the distribution $S(D)$ continuously evolves from the nozzle exit down to the spray region. This evolution describes the whole atomization mechanism. Being presented in a log–log scale, Fig. 2 is equivalent to a Richardson–Mandelbrot plot. As explained above, the examination of the local slope of this plot informs on the fractal property of the system (see Eq. (16)). We

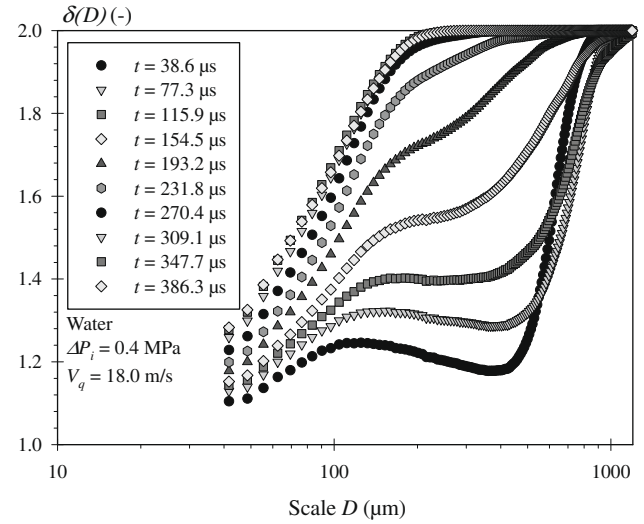

Fig. 4. Temporal evolution of the scale-dependent fractal dimension δ (water, $\Delta P_i = 0.4$ MPa, $t_0 = 115.9$ µs, $D_{0Spray} = 219$ µm).

calculated the local slope $LS(D)$ for each time and deduced the function $\delta(D)$ defined by:

$$\delta(D) = 2 - LS(D) \tag{17}$$

In agreement with the EDM method, this function is the local fractal dimension in the scale space (see Eq. (16)). Fig. 4 shows the local fractal dimension as a function of time for the situation corresponding to Fig. 2. The local fractal dimension evolves from 1 to 2 when covering the liquid system scale range. For times less than 200 μs, $\delta(D)$ first increases with D, reaches a plateau whose inclination increases with time, and sharply increases to reach 2 at $D = D_0$. Within the scale interval where the plateau is perceptible, the local fractal dimension is almost independent of the scale denoting a fractal property of the system in these scale and time intervals. This fractal property characterizes the tortuosity of the interface and ignores the system as a whole (Grout et al. 2007), and the corresponding fractal dimension is a textural fractal dimension as defined by Kaye (1989). It was reported (Grout et al. 2007) that this fractal dimension correlates with the liquid Reynolds number evidencing the impact of turbulence on the liquid sheet edge tortuosity in the near nozzle region. For times greater than 200 μs, the plateau is not perceptible anymore and $\delta(D)$ monotonously increases. For times greater than 300 μs, $\delta(D)$ stabilizes as well as the distribution $S(D)$ in Fig. 2: these functions characterize the final spray.

The results in Figs. 2 and 4 were obtained with a 200 pixels (700 μm) height Analyzing Window. This height belongs to the scale range covered by the liquid system when $t < 200$ μs and the increase of $\delta(D)$ towards 2 spreads on this particular value. An influence of the Analyzing Window height on the results must be suspected and investigated. For the nearest position of the Analyzing Window ($d_{AW} = 0.7$ mm) Fig. 5 shows the function $\delta(D)$ in the scale range [100 μm; 1000 μm] as a function of the Analyzing Window height h_{AW}. When $h_{AW} > 200$ pixels (700 μm), the increase of $\delta(D)$ spreads over a larger and larger scale range as h_{AW} increases. When h_{AW} increases, the Analyzing Window catches thinner and larger sections of the continuous liquid system (above and under the window, respectively) and consequently extends the scale range covered by the whole object. This dependency should be interpreted as a lack of analysis localness.

When $h_{AW} \leqslant 200$ pixels, $\delta(D)$ losses its dependency with this parameter: the scale range over which $\delta(D)$ increases remains unaffected by any modification of the Analyzing Window height. This means that this specific scale range is representative of the temporal variation of the liquid system at this particular position. This temporal variation is caught here thanks to the analysis of 150 images. In other words, the asymptotic function $\delta(D)$ obtained for sufficiently small Analyzing Window height is a signature of the intermittency of the atomization mechanism. The work was conducted with a constant Analyzing Window height equal to 200 pixels.

The results presented in Fig. 4 shows that the evolution of the liquid system morphology during the atomization mechanism is characterized by a scale and time-dependent fractal dimension. The model presented in Section 2 (Eq. (9)) was established for such situations and should be considered to describe the experimental observations.

The present experimental work is based on image analysis, which imposes an embedding dimension d equal to 2. The comparison between Eqs. (3) and (16) shows that the function $\Sigma(D) = \ln(1/S(D))$ is equivalent to a scale entropy function. As shown in Fig. 4, the local fractal dimension $\delta(D)$ varies from 1 to 2. Thus, the function $\phi(D) = \delta(D) - 2$ varies from -1 to 0 and represents the scale entropy flux function in the scale space (see Eqs. (4)–(6)). Thus, the evolution of the scale distribution can be described by the

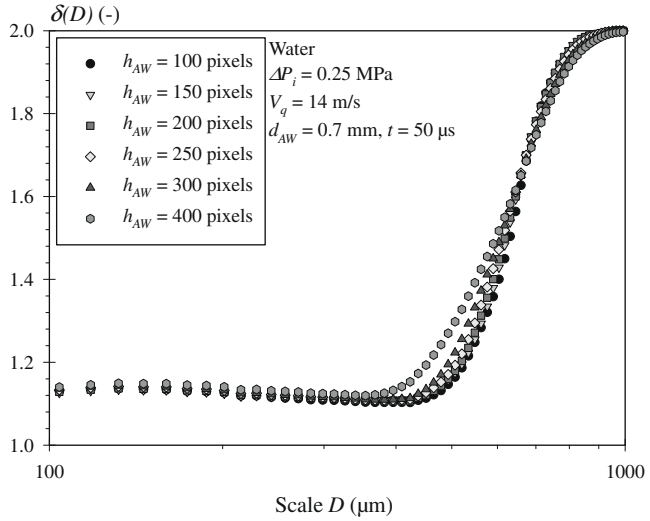

Fig. 5. Influence of the analyzing window height h_{AW} on the scale-dependent fractal dimension $\delta(D)$ (water, $\Delta P_i = 0.25$ MPa, $t = 50$ μs).

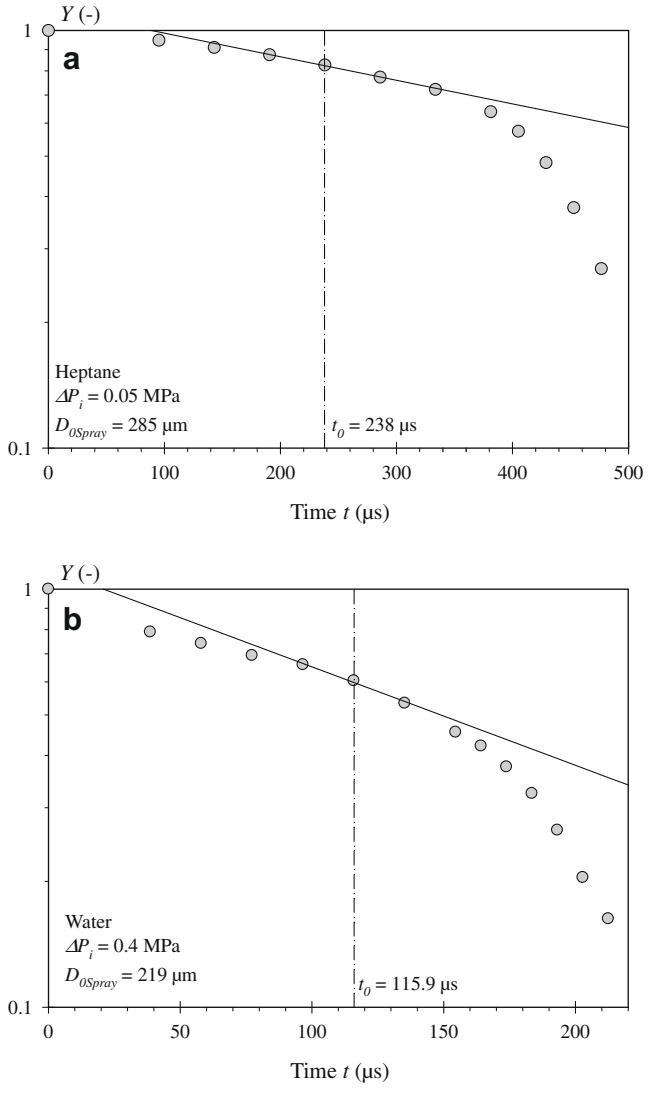

Fig. 6. Temporal evolution of Y for the spray reference scale D_{0Spray}. (a) Heptane, $\Delta P_i = 0.05$ MPa, $D_{0Spray} = 285$ μm, $t_0 = 238$ μs, and (b) water, $\Delta P_i = 0.4$ MPa, $D_{0Spray} = 219$ μm, $t_0 = 115.9$ μs.

diffusion equation (Eq. (9)). This equation introduces the scale diffusivity χ and the scale entropy flux sink $\omega(x,t)$ that are experimentally determined as follows.

As observed in Fig. 4, over a limited time interval and for a limited scale range, the fractal dimension is mainly a function of time, i.e., $\delta(D,t) \approx \delta(t)$. (This scale range is the one for which the liquid system boundary is fractal.) For these scales and during this time interval, the term $\partial^2\Sigma(x,t)/\partial x^2$ is much smaller than the two other terms in Eq. (9) and can be omitted. As demonstrated by Queiros-Conde (2003), the corresponding temporal evolution of the fractal dimension in this situation is given by Eq. (10). This equation can be rewritten as:

$$\ln(Y) = -\frac{t}{\tau^*} \tag{18}$$

where

$$Y = \frac{\delta(t) - \delta_0}{\delta(t=0) - \delta_0} \tag{19}$$

This simplified solution is applicable in a scale range and in a time interval provided that 1 – the fractal dimension in this scale range is mainly a function of time ($\delta(D,t) \approx \delta(t)$), 2 – the fractal dimension of these scales tends towards δ_0 as time increases (see Eqs. (18) and (19)), and 3 – the reference scale of the system is constant during the time interval ($dD_0/dt = 0$). The present results show that these assumptions are satisfied by the scale D_{0Spray} (reference scale of the spray) around the time t_0 (time at which the system reference scale is maximum). First, at time t_0, the scale D_{0Spray} always belongs to the scale range where fractality is observed (see Fig. 4 for instance). Thus, the first assumption is satisfied. Second, by definition, the fractal dimension of the spray reference scale tends towards δ_0 when time increases as required by the second assumption. Third, by definition, $dD_0/dt = 0$ at $t = t_0$ and it can be seen in Fig. 3 that, around t_0, the system reference scale (D_{0Max}) moderately varies with time. The third assumption is satisfied. In consequence, the temporal variation of the fractal dimension at scale D_{0Spray} around time t_0 should follow the linear dependence expressed by Eq. (18) and should allow the determination of the characteristic time τ^*.

For each working condition, the function Y is calculated for the reference scale of the spray D_{0Spray}, i.e., the time-dependent fractal dimension in Eq. (19) corresponds to the dimension measured for this scale as a function of time. Furthermore, $\delta(t=0)$ is taken equal to 1 since the liquid system is not deformed at the nozzle exit. The function Y is then plotted as a function of time in a semi-log graph. Such graphs are presented in Fig. 6a and b for different operating conditions. As expected, these figures show that the function Y is always less than 1 and monotonously decreases as time increases. The time t_0 is indicated in these graphs. As explained above and according to Eq. (18), the linearity between $\ln(Y)$ and t around time t_0 should provide the characteristic time τ^*. Therefore, a linear correlation is calculated in the $Y = f(t)$ plots using three points, namely, $Y(t_0)$ and the values of Y for the preceding and the following times. These linear regressions are shown in Fig. 6a and b. In all the situations, the three points used to calculate the linear regression aligned well. This signifies that for the scale D_{0Spray} and around time t_0, the solution equation (10) of the reduced diffusion equation provides a good temporal evolution of the local fractal dimension. This observation validates the assumption and underlines a sufficient temporal resolution of the analysis. Furthermore, in many situations, it has been observed that the linear regression spreads over the triplet of points used for the calculation (see Fig. 6a for instance). According to Eq. (18), the slope of this linear regression gives the characteristic time τ^* from which the scale diffusivity χ can be obtained. Referring to Eq. (10), the scale diffusivity is given here by:

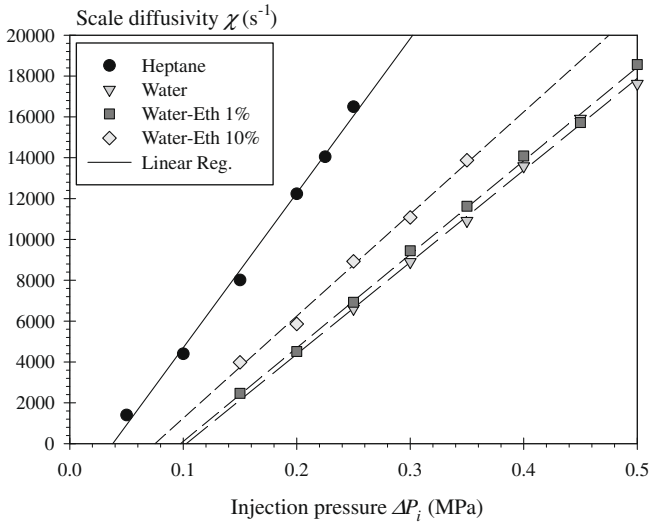

Fig. 7. Scale diffusivity χ versus the injection pressure (influence of the liquid properties).

$$\chi = \frac{\ln^2\left(\frac{D_{0Spray}}{D_{0Max}}\right)}{\tau^*} \tag{20}$$

Fig. 7 presents the scale diffusivity as a function of the injection pressure for all working conditions. The figure shows a strong organization of this parameter with the injection pressure as well as with the liquid physical properties. The scale diffusivity increases with the injection pressure. Increasing the injection pressure is modeled here as an increasing diffusion dynamic, which describes a greatest propensity of producing small scales, and finally small drops. The same variation is observed when the liquid surface tension coefficient decreases. When this coefficient decreases, smaller liquid structures can develop, and an increase of the diffusion dynamic describes this behavior. The dependencies between the scale diffusivity and the injection pressure shown in Fig. 7 are linear for each fluid, i.e.:

$$\chi \propto \frac{\Delta P_i}{\mu^*} \tag{21}$$

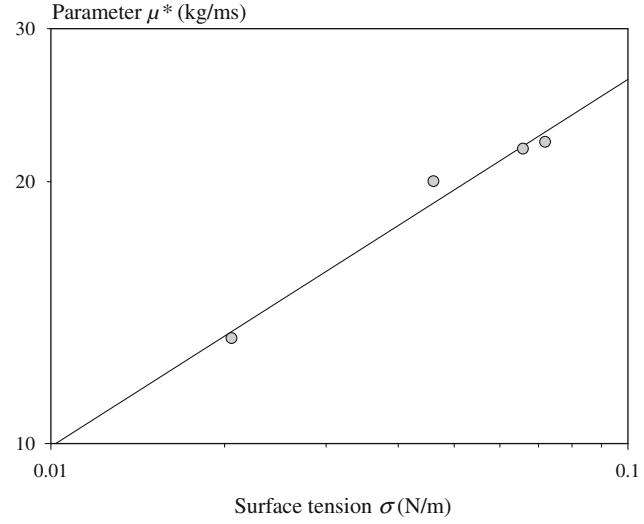

Fig. 8. Correlation between the parameter μ^* and the surface tension.

The coefficient μ^* introduced by Eq. (21) is dimensionally equivalent to a dynamic viscosity. It is calculated from the slope of the linear regressions shown in Fig. 7 and presented in Fig. 8 as a function of the liquid surface tension. This figure reports a strong correlation between μ^* and the surface tension coefficient. It has to be reminded that the surface tension forces mainly govern the atomization mechanism investigated here. It is therefore note surprising that the parameter μ^* that characterizes the dynamic of the liquid system shape evolution during the atomization mechanism correlates with the surface tension.

The diffusion model also introduces the scale entropy flux sink $\omega(x, t)$ that is defined by unit of scale logarithm. This function is also a characteristic of the atomization process. It can be determined by using the diffusion equation (Eq. (9)) and the scale diffusivity χ found. (We assume here that the scale diffusivity is independent of the scale.) Example of the scale entropy flux sink as a function of time is presented in Fig. 9. This figure also shows the corresponding evolution of the scale entropy $\Sigma(x, t) = \ln(1/S(x, t))$ and of the function $\phi(x, t) = \partial\Sigma(x, t)/\partial x = \delta(x, t) - 2$. The function $\phi(x, t)$ is negative indicating that the scale entropy flux is directed towards the increasing x. In Fig. 9, the variable x has been calculated by using the initial reference scale of the liquid system, i.e., the diameter d_{or} of the discharge orifice. The functions in Fig. 9 are presented for four times. The first time (38.6 μs) corresponds to the smallest distance between the nozzle and the analyzing window. The second time (115.9 μs) corresponds to the time t_0 for this operating condition. And the forth time (540.9 μs) is a time at which the diffusion process is completed. At each time,

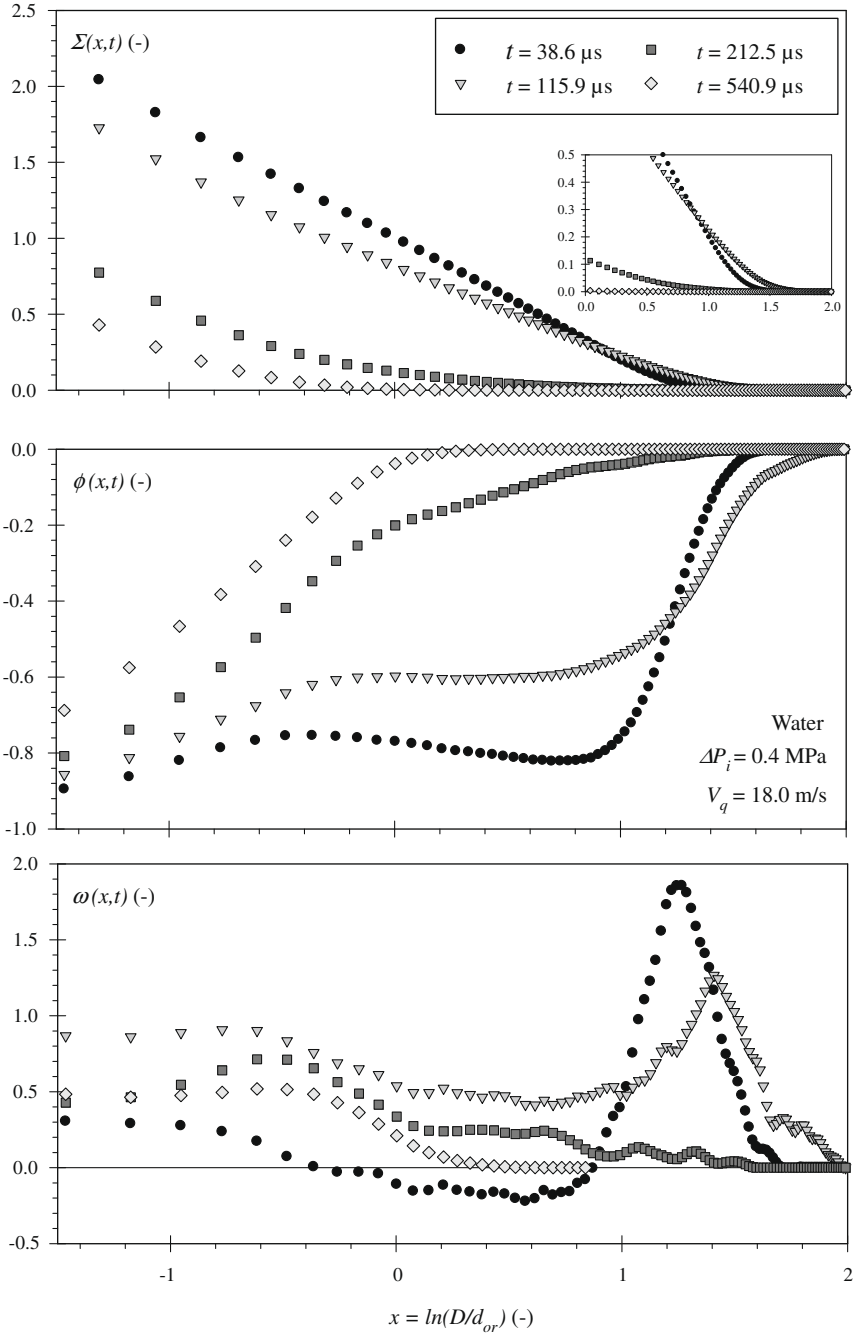

Fig. 9. Temporal evolution of the scale entropy (top), the scale entropy flux (middle) and the scale entropy flux sink (bottom) (water, $\Delta P_i = 0.4$ MPa).

the function $\omega(x,t)$ (bottom of Fig. 9) is mainly positive over the scale space: this indicates a lost of local scale entropy flux. For the smallest time shown in Fig. 9 (38.6 μs) we note that the scale entropy flux sink function is negative in the medium scale range. This characterizes a gain of scale entropy flux. This supplementary flux diffuses towards the increasing x following the scale entropy gradient and induces an increase of the scale entropy in the large scale and therefore an increase of the reference scale with time (see Fig. 9 top). The diffusion of this supplementary flux lasts until $t = t_0$. As explained above, the increase of the reference scale observed at the beginning of the process is due to the effect of the double-swirl structure of the flow issuing from the nozzle. This demonstrates that the function $\omega(x,t)$ carries information in relation with the issuing liquid flow.

At the end of the atomization process, the distribution of scale entropy in the scale space becomes independent of the time and the diffusion equation simplifies as Eq. (8). Making use of Eq. (6), it can be shown that, at this stage, the function $\omega(x)$ is normalized, i.e., it fulfills the following condition:

$$\int_{-\infty}^{+\infty} \omega(x)dx = 1 \tag{22}$$

We introduce here a new function $\omega(t)$ defined by:

$$\omega(t) = \int_{-\infty}^{+\infty} \omega(x,t)dx \tag{23}$$

At each time, $\omega(t)$ represents the total scale entropy flux lost over the whole scale space. Examples of this function are presented in Figs. 10 and 11. Fig. 10 shows $\omega(t)$ for water at four injection pressures. The first point to be noted is that for great time t, the limit 1 is almost reached. The slightly underestimated values of $\omega(t)$ for these times result from spatial resolution limitation: it can be seen in Fig. 9 that $\omega(x,t)$ is not closed in the small scale range. Fig. 10 shows that the total scale entropy flux lost during the atomization process increases, reaches a maximum and decreases towards the limit 1. This figure reports a clear correlation between $\omega(t)$ and the injection pressure; an increasing injection pressure being represented by a decrease of the total scale entropy flux loses over the scale space. At each time Fig. 11 also shows very organized $\omega(t)$ as a function of the liquid physical properties. In particular it can be seen that a sharp reduction of the surface tension induces a decrease of the maximum of $\omega(t)$. The results presented in Figs. 10 and 11 show that the production of finer sprays is accompanied by a global decrease of $\omega(t)$ (when ΔP_i increases or when σ decreases for instance). As shown in Fig. 7, this behavior is also related to an increase of the scale diffusivity. Thus, atomization efficiency improvement can be reached by increasing the propensity of the scale entropy to diffuse in the small scale, phenomenon that requires greater scale diffusivity and reduced lose of scale entropy flux. All these results demonstrate the relevance of scale entropy diffusion model to describe a liquid atomization process and encourage exploring this new way of apprehending liquid atomization and spray systems.

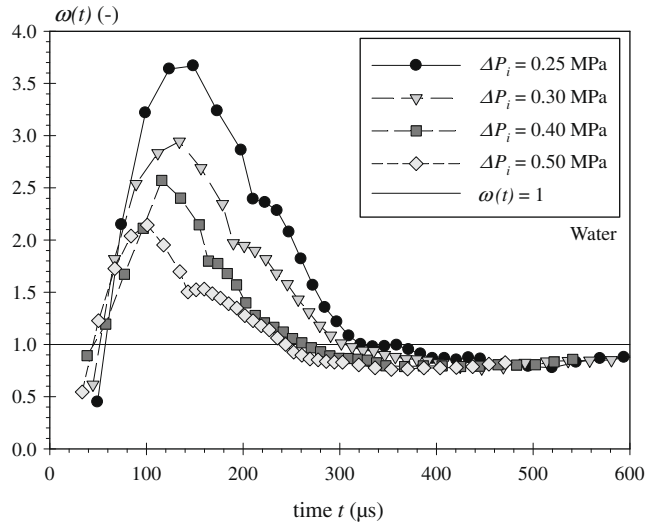

Fig. 10. Temporal evolution of the total scale entropy flux sink over the scale space (water, influence of the injection pressure).

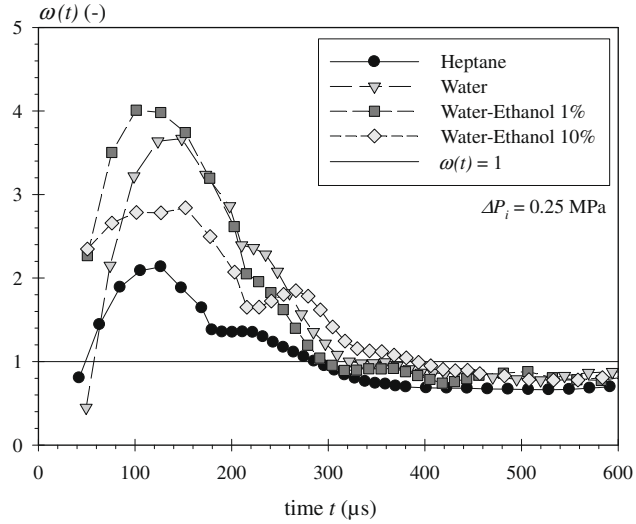

Fig. 11. Temporal evolution of the total scale entropy flux sink over the scale space (ΔP_i = 0.25 MPa, influence of the fluid).

5. Conclusion

This study presents the first attempt in applying the scale entropy diffusion model developed by Queiros-Conde (2003) to describe a liquid atomization process. During an atomization process, the shape of the liquid system continuously evolves. The model describes the evolution of this shape. The shape of the local liquid system is characterized by the scale entropy distribution in the scale space, distribution equivalent to the surface-based scale distribution introduced in previous works (Dumouchel et al. 2008a,b). The evolution of the scale entropy in the scale space is associated to a diffusion equation similar to a 1-D spatio-temporal heat diffusion equation. It therefore introduces a scale diffusivity, which characterizes the propensity of a scale to develop, as well as a scale entropy flux sink, which contributes to the local balance of scale entropy fluxes represented by the local fractal dimension. Both the scale diffusivity and the scale entropy flux sink are experimentally determined. This is the first time such measurements are performed. Correlations found between the operating conditions (injection pressure and liquid physical properties) and the diffusion characteristics (scale diffusivity and scale entropy flux sink) underline the relevance of this model to describe liquid atomization mechanism. Among other results, connections between the characteristic of the flow issuing from the nozzle and the scale entropy flux sink are evidenced. Therefore, the scale entropy diffusion model provides a new way of apprehending liquid atomization mechanisms and should be encouraged. This work also demonstrates the pertinence of the scale entropy diffusion model to describe physical processes involving shape evolution.

References

Bérubé, J., Jébrak, M., 1999. High precision boundary fractal analysis for shape characterization. Comput. Geosci. 25, 1059–1071.

Dumouchel, C., 2008. On the experimental investigation on primary atomization of liquid stream. Exp. Fluids 45, 371–422.

Dumouchel, C., Cousin, J., Triballier, K., 2005a. On the role of the liquid flow characteristics on low-Weber-number atomization processes. Exp. Fluids 38, 637–647.

Dumouchel, C., Cousin, J., Triballier, K., 2005b. Experimental analysis of liquid–gas interface at low-Weber-number: interface length and fractal dimension. Exp. Fluids 39, 651–666.

Dumouchel, C., Cousin, J., Grout, S., 2008a. Analysis of two-dimensional liquid spray images: the surface-based scale distribution. J. Flow Visual. Image Process. 15, 59–83.

Dumouchel, C., Grout, S., Cousin, J., 2008b. Application of surface-based scale distributions to characterize liquid sprays: influence of the liquid properties. In: Proceedings of the ILASS-Europe 2008, September 8–10, Como, Italy, Paper ID ILASS08-A091.

Grout, S., Dumouchel, C., Cousin, J., Nuglisch, H., 2007. Fractal analysis of atomizing liquid flows. Int. J. Multiphase Flows 33, 1023–1044.

Guessasma, S., Montavon, G., Coddet, C., 2003. On the implementation of the fractal concept to quantify thermal spray deposit characteristics. Surf. Coat. Technol. 173, 24–38.

Hunt, J.C.R., Vassilicos, J.C., 1991. Kolmogorov's contribution to the physical and geometrical understanding of small-scale turbulence and recent developments. Proc. R. Soc. Lond. A 434, 183–210.

Kaye, B.H., 1989. A Random Walk through Fractal Dimensions. VCH, New York.

Le Moyne, L., Freire, V., Queiros-Conde, D., 2008. Fractal dimension and scale entropy applications in a spray. Chaos, Solitons & Fractals 38, 696–704.

Mandelbrot, B., 1982. The Fractal Geometry of Nature. WH Freeman, New York.

Mansour, A., Chigier, N., 1991. Dynamic behavior of liquid sheets. Phys. Fluids 3, 2971–2980.

Panico, J., Sterling, P., 1995. Retinal neurons and vessels are not fractal but space-filling. J. Comp. Neurol. 361, 479–490.

Queiros-Conde, D., 1999. Geometry of intermittency in fully developed turbulence. C. R. Acad. Sci. Paris Ser. IIb 327, 1385–1390.

Queiros-Conde, D., 2000. Entropic skins model in fully developed turbulence. C. R. Acad. Sci. Paris Ser. IIb 328, 541–546.

Queiros-Conde, D., 2001. Internal geometry in the multifractal spectrum in fully developed turbulence. Phys. Rev. E 64, 015301.

Queiros-Conde, D., 2003. A diffusion equation to describe sacle- and time-dependent dimensions of turbulent interfaces. Proc. R. Soc. Lond. A 459, 3043–3059.

Rizk, N.K., Lefebvre, A.H., 1984. Influence of downstream distance on simplex atomizer spray characteristics, ASME 84-WA/HT-25.

Shavit, U., Chigier, N., 1995. Fractal dimensions of liquid jet interface under break-up. Atom. Sprays. 5, 525–543.

Sreenivasan, K.R., Meneveau, C., 1986. The fractal facets of turbulence. J. Fract. Mech. 173, 357–386.

Yon, J., Lalizel, G., Blaisot, J.B., 2004. A statistical morphological determination of the growth rate of the interfacial disturbance of an excited Rayleigh jet. J. Flow Visual. Image Process. 11, 1–17.